Medium-density amorphous ice

Alexander Rosu-Finsen[1], Michael B. Davies[2,3], Alfred Amon[1], Andrea Sella[1], Angelos Michaelides[3,2]*, Christoph G. Salzmann[1]*

Affiliations:

[1] Department of Chemistry, University College London; London, WC1H 0AJ, United Kingdom.

[2] Department of Physics and Astronomy, University College London; London, WC1E 6BT, United Kingdom.

[3] Yusuf Hamied Department of Chemistry, University of Cambridge; Cambridge, CB2 1EW, United Kingdom.

*Corresponding authors. Email: c.salzmann@ucl.ac.uk, am452@cam.ac.uk

Abstract:

The amorphous ices govern a wide range of cosmological processes and are potentially key materials for explaining the anomalies of liquid water. A substantial density gap between low-density amorphous (LDA) and the high-density amorphous ices (HDA) with liquid water in the middle is a cornerstone of our current understanding of water. However, here we show that ball milling 'ordinary' ice I*h* at low temperature gives a structurally distinct medium-density amorphous ice (MDA) within this density gap. These results raise the possibility that MDA is the true glassy state of liquid water or alternatively a heavily sheared crystalline state. Remarkably, the compression of MDA at low temperature leads to a sharp increase of its recrystallization enthalpy highlighting that H_2O can be a high-energy geophysical material.

One-Sentence Summary: Shaken, not stirred: Ball milling gives amorphous ice in the density range of liquid water.

Main Text:

Water has a remarkably rich and fascinating phase diagram with 20 crystalline phases and at least two families of amorphous forms.(*1-7*) While three new crystalline phases have been discovered in the last five years alone,(*2-6*) the discovery of novel amorphous states is much less common. The current complement of amorphous forms comprises low-density amorphous ice (LDA), first made through vapor deposition in the 1930s.(*8*) By compression of ice I*h* or LDA at low temperatures, high-density amorphous ice (HDA) was made in the 1980s.(*9, 10*) Heating HDA under pressure gives either expanded high-density (eHDA) or very high-density amorphous ice (vHDA), as reported in the early years of this century.(*11, 12*) As their names suggest, amorphous ices are distinguished principally by their densities, with LDA having a density of 0.94 g cm^{-3} and the HDAs starting from 1.13 g cm^{-3} at ambient pressure and 77 K.(*7*) This leaves a conspicuous gap in densities around the density of liquid water (1 g cm^{-3}) which is not filled by any known crystalline phases and it is unknown if amorphous ice can display a density in this gap. This gap and the question if the amorphous ices have corresponding liquid states below a liquid-liquid critical point is a topic of great interest with respect to explaining water's many anomalies.(*13-23*) The fact that amorphous ice is the most common form of ice in the Universe(*24*) underpins the need to understand the structurally disordered states of H_2O.

Aside from the previously reported techniques for making amorphous ices, ball milling is an established technique for making amorphous materials in general. It is widely used in the fields of metallic alloys and pharmaceuticals but has not yet been applied to ice.(*25, 26*) At the heart of the amorphization processes are ball-crystal-ball impact events that exert a combination of compressive and shear forces on the crystalline starting materials as shown schematically in Fig. 1A. While local melting effects have been discussed as the origin for amorphization, the introduction of dislocation defects seems to be the main driving force.(*27*) In general, the amorphization through ball milling is most effective at low temperatures.(*28*)

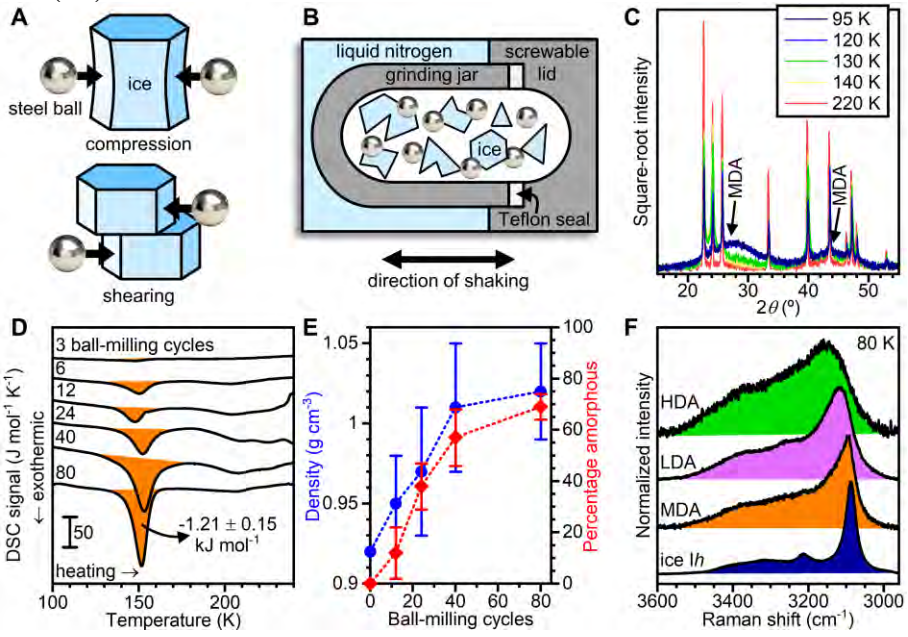

Fig. 1. Preparation and physical properties of medium-density amorphous ice (MDA). (**A**) Illustration of the ball-crystal-ball impact events upon ball milling. (**B**) Schematic of the low-temperature ball-milling setup. (**C**) X-ray diffraction patterns (square-root intensities) upon

heating MDA after 80 ball-milling cycles. (**D**) Differential scanning calorimetry of ice ball-milled for increasing numbers of ball-milling cycles. (**E**) Density (blue circles) and percentage amorphous content (red diamonds) at 77 K as a function of the ball-milling cycles. The error bars reflect the standard deviation from at least three measurements. (**F**) Comparison of the Raman spectra of HDA, LDA, MDA and ice I*h* at 80 K in the O-H stretching spectral region.

Here we show that low-temperature ball milling of ice I*h* leads to amorphous ice with a density in the gap between LDA and HDA. A schematic of the experimental setup is shown in Fig. 1B. The grinding jar is cooled to 77 K with liquid nitrogen, filled with ice and stainless-steel balls, and firmly closed. To achieve the amorphization, the entire assembly is shaken vigorously for a range of ball-milling cycles. Full details of the experimental procedure are given in the Supplementary Materials.

The formation of amorphous ice after 80 ball-milling cycles can be seen from the broad X-ray diffraction features in Fig. 1C with peak maxima at 27.2 and 43.7 degrees. The shift of the first strong diffraction feature (FSDF) at 27.2 degrees away from the most intense Bragg peaks of ice I*h* signifies major structural changes. For comparison, cryogenic ball milling of the isostructural NH_4F I*h* results in the broadening without shifting of the Bragg peaks indicating only a reduction of the crystallite sizes (Fig. S1). A comparison with the diffraction patterns of all currently known amorphous ices in Fig. S2 highlights that the amorphous ice obtained through ball milling is structurally unique. The closest match in terms of peak positions is HDA. Yet, in contrast to HDA,(*10*) the ball-milled amorphous ice does not transform to LDA upon heating at ambient pressure (Fig. 1C). Instead, the diffraction patterns collected upon heating show recrystallization to stacking disordered ice I (ice I*sd*) above ~140 K which later transforms to the stable ice I*h*. A quantitative analysis of the cubic/hexagonal stacking disorder in the ice I*sd* using the MCDIFFaX software(*29*) is presented in Fig. S3. The ice I*sd* obtained from the ball-milled ice contains 31% cubic stacking. It is interesting to note that the amorphous ice does not recrystallize to the fully hexagonal ice I*h* starting material which underpins the fact that the ice undergoes substantial structural changes upon amorphization. Optical images of the ball-milled ice after 80 milling cycles show irregularly-shaped particles with diameters in the range of several tens of micrometers (Fig. S4).

The progress of the ball milling was monitored quantitatively with differential scanning calorimetry (DSC). Fig. 1D shows DSC scans of ball-milled samples with increasing numbers of ball-milling cycles. The recrystallization of the amorphous ice manifests as an exothermic phase transition at ~150 K which increases in area with increasing milling cycles. An enthalpy of -1.16 ± 0.09 kJ mol^{-1} is obtained after 40 milling cycles. Further increase to 80 milling cycles gives a heat release of -1.21 ± 0.15 kJ mol^{-1} indicating that the amorphization process is close to completion after 40 milling cycles. The areas of the exotherms are independent of the diameters of the steel balls in the 10 to 20 mm range as shown in Fig. S5 illustrating that the amorphization process takes place robustly within a range of different ball-milling conditions.

The progressive amorphization upon balling milling was also followed quantitatively by fully crystallizing the amorphous samples through heating and analyzing the changes in the intensities of the ice I*h* Bragg peaks. Even after 80 ball-milling cycles, the X-ray diffraction pattern shows Bragg peaks of ice I*h* (Fig. 1C and Fig. S6). This contamination

might be due to incomplete amorphization but could also arise from vapor condensation during sample recovery and transfer. Consistent with the increases in the areas of the exotherms (Fig. 1D), the percentages of the amorphous content from the X-ray diffraction analysis increase steadily up to 40 milling cycles and then level off at around 70% (Fig. 1E). Due to the possible contamination of the samples through vapor condensation, this value represents the lower limit of the amorphous content.

The bulk densities of the ball-milled samples were determined using buoyancy measurements in liquid nitrogen. Fig. 1E shows that the samples become denser as the amorphization progresses closely following the trend of the amorphous content. After 80 milling cycles, the ball-milled ice has a density of 1.02 ± 0.03 g cm^{-3} at 77 K. Considering that the sample is at least 70% amorphous means that the amorphous fraction of the sample has a density in the 1.02 to 1.06 g cm^{-3} range. This density range falls into the gap between LDA (0.94 g cm^{-3}) and HDA (1.15 g cm^{-3}).(*10, 12*) The amorphous ice obtained from ball milling is therefore named medium-density amorphous ice (MDA).

The Raman spectrum of MDA in the spectral range of the O-H stretching modes is shown in Fig. 1F. While the X-ray diffraction data of MDA was closest to HDA, it is interesting that the Raman spectrum of MDA is closer to LDA than to HDA.

The structural mechanism of the amorphization process through ball milling was investigated computationally. As shown schematically in Fig. 2A and Fig. S7, the computational protocol started with a periodically repeated ice I*h* simulation box containing 2880 water molecules that was subjected to random shearing of layers followed by geometry optimization of the local molecular environments. These steps were repeated until the calculated structure factors and other structural characteristics converged (Figs S8-9). The details of the computational approach are given in the Supplementary Materials. The robustness of the computational approach in terms of the path independence and system size is demonstrated in Figs S10-11.

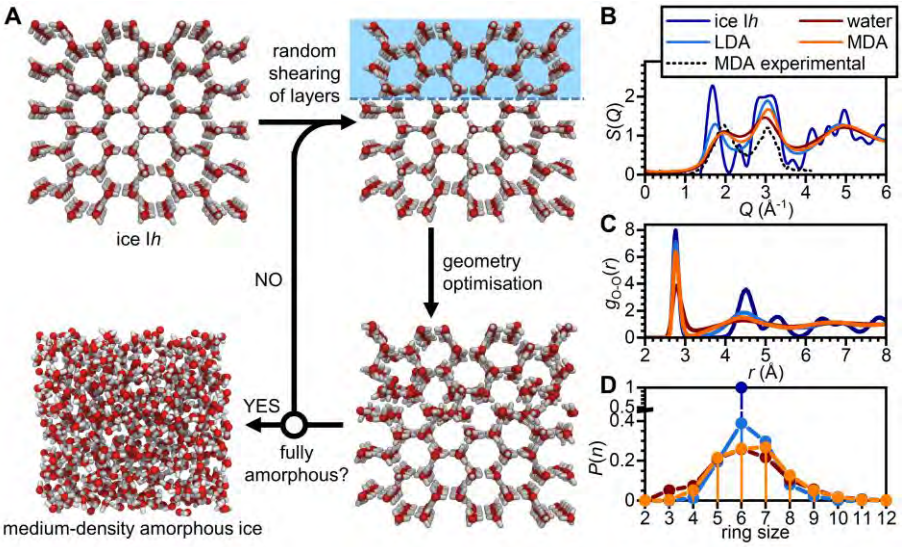

Fig. 2. Computational investigation into the mechanism of formation of MDA. (**A**) Schematic of the computational protocol that yields MDA upon repeated shearing and geometry-optimization steps. (**B**) Experimental and computational X-ray structure factors, $S(Q)$, of MDA, water, LDA and ice I*h*. (**C**) Corresponding oxygen-oxygen pair distributions functions, $g_{O\text{-}O}(r)$,

and (**D**) primitive ring-size distributions. All simulations were carried out with periodic boundary conditions and 2,880 water molecules.

During the computational amorphization process, a density increase from 0.92 to 0.97 g cm^{-3} was found similar to the experimental observations (Fig. S12). Furthermore, there is good agreement between the calculated and experimental diffraction patterns of MDA in terms of the peak positions of the diffraction features as shown in Fig. 2B. This illustrates that dislocation processes are indeed essential for achieving the amorphization of ice I*h* to the denser MDA. Structurally speaking, the amorphization process goes along with a partial collapse of the second coordination shell of the water molecules as illustrated in Fig. 2C. This means that not hydrogen-bonded water molecules move towards the first coordination shell which is a well-known structural mechanism for achieving higher densities in ice.(*1, 30*)

Interestingly, the computational structure of MDA is closer to liquid water than to LDA. In Fig. 2B, this can be seen from the positions of the FSDFs which are indicators for the intermediate-range structure. The FSDFs of MDA and liquid water are found at similar positions whereas the FSDF of LDA is close to ice I*h*. From the oxygen-oxygen pair-distribution functions in Fig. 2C, a progressive collapse of the second coordination shell is observed upon going from ice I*h* to LDA, to MDA, and to liquid water. The same progression can also be seen in the statistics of the primitive ring sizes (Fig. 2D).

The experimental identification of MDA shows that the polyamorphism of H_2O, the existence of multiple distinct amorphous states, is more complex than previously appreciated. A key question is whether MDA should be regarded as a glassy state of liquid water. As mentioned earlier, the glassy natures of LDA and HDA are still debated which means that a range of different scenarios are now possible with MDA joining the fray. A fascinating possibility is that MDA represents the glass of liquid water in agreement with their similar densities and diffraction characteristics.(*31*) This would not necessarily violate the well-known liquid-liquid critical point hypothesis,(*13, 14, 17, 21, 23*) but MDA would need to have a glass transition temperature above the liquid-liquid critical point. Accordingly, MDA would represent liquid water before the phase separation into LDA and HDA takes place at temperatures below the liquid-liquid critical point. Consistent with this scenario, MDA does not show a glass transition below the recrystallization temperature at ~150 K despite extensive annealing at a range of different temperatures (Fig. S13). According to this scenario, MDA would be metastable with respect to either LDA or HDA at low temperatures and at all pressures.

Alternatively, a pressure range might exist at low temperatures within which MDA is more stable than LDA and HDA. However, due to the generally slow kinetics at low temperatures, the two scenarios are difficult to distinguish. Heating MDA at ambient pressure does not lead to the formation of LDA (Fig. 1C) and MDA remained stable upon heating to the *p*/*T* conditions of eHDA (Fig. S14). The uniaxial compression of MDA on the other hand at 77 K shows a transition to HDA with a step-wise change in volume at an onset pressure of about 1.1 GPa (Fig. 3A). Consistent with the higher density of MDA compared to ice I*h*, the step-wise change in volume is smaller compared to the corresponding transition of the same amount of ice I*h*. The onset pressure of the MDA to HDA transition upon compression is at

considerably higher pressures than the LDA to HDA transition which is found at about 0.5 GPa.(*32*)

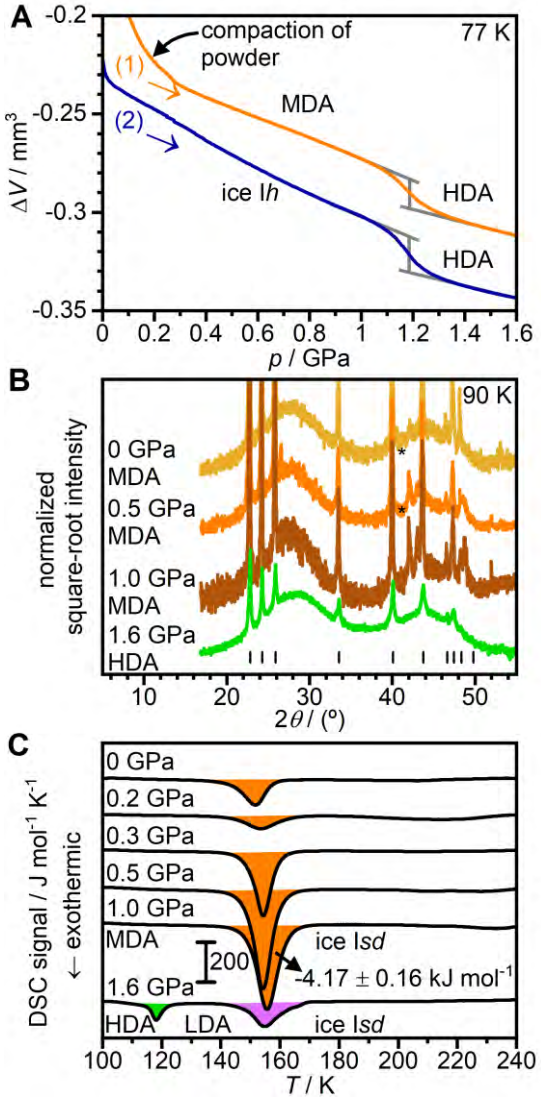

Fig. 3. Effect of pressure on MDA. (**A**) In-situ volume changes upon compression of equal amounts of MDA and ice I*h* to 1.6 GPa at 77 K. Grey lines indicate the step-wise volume changes during the transition to HDA. (**B**) X-ray diffraction patterns at 90 K and ambient pressure after compression of MDA to the indicated pressures at 77 K. (**C**) Differential scanning calorimetry (DSC) scans upon heating at 10 K min^{-1} at ambient pressure after compression of MDA at 77 K. The X-ray diffraction patterns and DSC scans after compression to 1.6 GPa correspond to HDA.

A third scenario is that MDA is not a glassy liquid but a heavily sheared crystalline state that lacks a connection with the liquid phase. Whatever the precise structural nature of MDA is, it is expected to play an important role in the geology of ice at low temperatures, for example, in the many ice moons of the Solar system and beyond. Tidal forces in the interiors of ice moons induced by the gravitational forces of gas giants may cause similar shear forces as found in ball milling and could hence facilitate the transition of ice I*h* to MDA.

Finally, we note that MDA displays one remarkable property that is not found for any of the other amorphous or crystalline forms of ice. The X-ray diffraction patterns in Fig. 3B show that the structure of MDA remains unchanged upon compression at 77 K up to 1.0 GPa. Yet, the area of the recrystallization exotherm upon heating at ambient pressure increases substantially from –1.21 ± 0.15 kJ mol^{-1} for the uncompressed material to –4.02 ± 0.14 kJ mol^{-1} after compression to 0.5 GPa. Compression to 1.0 GPa leads to a further small increase to –4.17 ± 0.16 kJ mol^{-1}. This is an extraordinarily large amount of heat that corresponds to about 70% of the heat released upon freezing liquid water to ice I*h*. Since MDA is prepared through ball milling, the amorphous sample is expected to display a high surface area. Given that the X-ray diffraction data remains unchanged upon compression, the increase in the recrystallization enthalpy can be rationalized by the formation of pressure-induced strain at the grain boundaries as it has been observed for metals.(*33*) Similar processes could take place in the ice layers of ice moons as they are subjected to tidal forces and heat releases from the recrystallization of MDA could play a role in activating tectonic motions.

The identification of MDA shows that H_2O is more complex at low temperatures than previously appreciated. The possibility that MDA may represent the true glass of liquid water is an exciting prospect that would have far reaching consequences for our understanding of liquid water and its many anomalies. Any valid model of water should be able to explain the existence of MDA and its relationship with LDA and HDA. Regardless of the exact nature of MDA, it has the remarkable ability to store mechanical energy from compression which is released upon heating at low pressure. Identifying and establishing how abundant and geophysically active MDA is in the Solar system and beyond is an exciting prospect.

References

1. C. G. Salzmann, Advances in the Experimental Exploration of Water's Phase Diagram. *J. Chem. Phys.* **150**, 060901 (2019).
2. M. Millot *et al.*, Nanosecond X-ray Diffraction of Shock-compressed Superionic Water Ice. *Nature* **569**, 251-255 (2019).
3. R. Yamane *et al.*, Experimental evidence for the existence of a second partially-ordered phase of ice VI. *Nat. Comm.* **12**, 1129 (2021).
4. C. G. Salzmann, J. S. Loveday, A. Rosu-Finsen, C. L. Bull, Structure and nature of ice XIX. *Nat. Comm.* **12**, 3162 (2021).
5. T. M. Gasser, A. V. Thoeny, A. D. Fortes, T. Loerting, Structural characterization of ice XIX as the second polymorph related to ice VI. *Nat. Comm.* **12**, 1128 (2021).
6. V. B. Prakapenka, N. Holtgrewe, S. S. Lobanov, A. F. Goncharov, Structure and properties of two superionic ice phases. *Nat. Phys.* **17**, 1233-1238 (2021).
7. T. Loerting *et al.*, How Many Amorphous Ices Are There? *Phys. Chem. Chem. Phys.* **13**, 8783-8794 (2011).
8. E. F. Burton, W. F. Oliver, The Crystal Structure of Ice at Low Temperatures. *Proc. R. Soc. London, Ser. A* **153**, 166-172 (1935).
9. O. Mishima, L. D. Calvert, E. Whalley, 'Melting Ice' I at 77 K and 10 kbar: A New Method of Making Amorphous Solids. *Nature* **310**, 393-395 (1984).
10. O. Mishima, L. D. Calvert, E. Whalley, An Apparently First-order Transition Between Two Amorphous Phases of Ice Induced by Pressure. *Nature* **314**, 76-78 (1985).
11. R. J. Nelmes *et al.*, Annealed High-density Amorphous Ice Under Pressure. *Nat. Phys.* **2**, 414-418 (2006).

12. T. Loerting, C. Salzmann, I. Kohl, E. Mayer, A. Hallbrucker, A Second Distinct Structural "State" of High-density Amorphous Ice at 77 K and 1 bar. *Phys. Chem. Chem. Phys.* **3**, 5355-5357 (2001).
13. P. H. Poole, F. Sciortino, U. Essmann, H. E. Stanley, Phase Behavior of Supercooled Water. *Nature* **360**, 324-328 (1992).
14. O. Mishima, H. E. Stanley, Decompression-induced melting of ice IV and the liquid-liquid transition in water. *Nature* **392**, 164-168 (1998).
15. J. S. Tse *et al.*, The Mechanisms for Pressure-induced Amorphization of Ice Ih. *Nature* **400**, 647-649 (1999).
16. H. Schober *et al.*, Crystal-like High Frequency Phonons in the Amorphous Phases of Solid Water. *Phys. Rev. Lett.* **85**, 4100-4103 (2000).
17. P. G. Debenedetti, Supercooled and glassy water. *J. Phys.: Condens. Matter* **15**, R1669–R1726 (2003).
18. B. Geil, M. M. Koza, F. Fujara, H. Schober, F. Natali, Absence of Fast Precursor Dynamics of Low-density Amorphous Ice around its Hypothetical Glass Transition Temperature. *Phys. Chem. Chem. Phys.* **6**, 677-679 (2004).
19. D. T. Limmer, D. Chandler, Theory of Amorphous Ices. *Proc. Natl. Acad. Sci. USA* **111**, 9413-9418 (2014).
20. J. J. Shephard *et al.*, Is High-Density Amorphous Ice Simply a "Derailed" State along the Ice I to Ice IV Pathway? *J. Phys. Chem. Lett.* **8**, 1645-1650 (2017).
21. P. G. Debenedetti, F. Sciortino, G. H. Zerze, Second critical point in two realistic models of water. *Science* **369**, 289-292 (2020).
22. C. A. Tulk, J. J. Molaison, A. R. Makhluf, C. E. Manning, D. D. Klug, Absence of amorphous forms when ice is compressed at low temperature. *Nature* **569**, 542-545 (2019).
23. K. H. Kim *et al.*, Experimental observation of the liquid-liquid transition in bulk supercooled water under pressure. *Science* **370**, 978-982 (2020).
24. S. Kwok, *Physics and Chemistry of the Interstellar Medium*. (University Science Books, Sausalito, USA, 2007).
25. A. W. Weeber, H. Bakker, Amorphization by ball milling. A review. *Physica B Condens. Matter* **153**, 93-135 (1988).
26. M. Descamps, J. F. Willart, Perspectives on the amorphisation/milling relationship in pharmaceutical materials. *Adv. Drug Deliv. Rev.* **100**, 51-66 (2016).
27. F. Delogu, G. Cocco, Weakness of the "hot spots" approach to the kinetics of mechanically induced phase transformations. *J. Alloys Compd.* **465**, 540-546 (2008).
28. M. Descamps, J. F. Willart, E. Dudognon, V. Caron, Transformation of Pharmaceutical Compounds upon Milling and Comilling: The Role of T_g. *J. Pharm. Sci.* **96**, 1398-1407 (2007).
29. T. L. Malkin *et al.*, Stacking Disorder in Ice I. *Phys. Chem. Chem. Phys.* **17**, 60-76 (2015).
30. J. L. Finney, A. Hallbrucker, I. Kohl, A. K. Soper, D. T. Bowron, Structures of High and Low Density Amorphous Ice by Neutron Diffraction. *Phys. Rev. Lett.* **88**, 22503-22501 (2002).
31. N. Esmaeildoost *et al.*, Anomalous temperature dependence of the experimental x-ray structure factor of supercooled water. *J. Chem. Phys.* **155**, 214501 (2021).
32. O. Mishima, Reversible First-order Transition between Two H_2O Amorphs at 0.2 GPa and 135 K. *J. Chem. Phys.* **100**, 5910-5912 (1994).
33. H. Gleiter, Nanocrystalline materials. *Prog. Mater. Sci.* **33**, 223-315 (1989).

34. A. B. Spierings, M. Schneider, R. Eggenberger, Comparison of density measurement techniques for additive manufactured metallic parts. *Rapid Prototyp. J.* **17**, 380-386 (2011).
35. K. Röttger, A. Endriss, J. Ihringer, S. Doyle, W. F. Kuhs, Lattice Constants and Thermal Expansion of H_2O and D_2O Ice Ih Between 10 and 265 K. *Acta Cryst.* **B50**, 644-648 (1994).
36. B. Kamb, Ice II: A Proton-Ordered Form of Ice. *Acta Cryst.* **17**, 1437-1449 (1964).
37. E. Mayer, R. Pletzer, Astrophysical Implications of Amorphous Ice - a Microporous Solid. *Nature* **319**, 298-301 (1986).
38. S. K. Talewar *et al.*, Gaseous "Nanoprobes" for Detecting Gas-trapping Environments in Macroscopic Films of Vapor-deposited Amorphous Ice. *J. Chem. Phys.* **151**, 134505 (2019).
39. T. Loerting *et al.*, How Many Amorphous Ices Are There? *Phys. Chem. Chem. Phys.* **13**, 8783-8794 (2011).
40. A. Hallbrucker, E. Mayer, Calorimetric Study of the Vitrified Liquid Water to Cubic Ice Phase Transition. *J. Phys. Chem.* **91**, 503-505 (1987).
41. O. Mishima, L. D. Calvert, E. Whalley, 'Melting Ice' I at 77 K and 10 kbar: A New Method of Making Amorphous Solids. *Nature* **310**, 393-395 (1984).
42. T. Loerting, C. Salzmann, I. Kohl, E. Mayer, A. Hallbrucker, A Second Distinct Structural "State" of High-density Amorphous Ice at 77 K and 1 bar. *Phys. Chem. Chem. Phys.* **3**, 5355-5357 (2001).
43. R. J. Nelmes *et al.*, Annealed High-density Amorphous Ice Under Pressure. *Nat. Phys.* **2**, 414-418 (2006).
44. T. L. Malkin *et al.*, Stacking Disorder in Ice I. *Phys. Chem. Chem. Phys.* **17**, 60-76 (2015).
45. C. G. Salzmann, B. J. Murray, J. J. Shephard, Extent of stacking disorder in diamond. *Diam. Relat. Mater.* **59**, 69-72 (2015).
46. J. L. F. Abascal, E. Sanz, R. García Fernández, C. Vega, A potential model for the study of ices and amorphous water: TIP4P/Ice. *J. Chem. Phys.* **122**, 234511 (2005).
47. M. Matsumoto, T. Yagasaki, H. Tanaka, Novel Algorithm to Generate Hydrogen-Disordered Ice Structures. *J. Chem. Inf. Model.* **61**, 2542-2546 (2021).
48. A. Hjorth Larsen *et al.*, The atomic simulation environment—a Python library for working with atoms. *J. Phys.: Condens. Matter* **29**, 273002 (2017).
49. S. Plimpton, Fast Parallel Algorithms for Short-Range Molecular Dynamics. *J. Comp. Phys.* **117**, 1-19 (1995).
50. S. Le Roux, P. Jund, Ring statistics analysis of topological networks: New approach and application to amorphous GeS2 and SiO2 systems. *Comput. Mater. Sci.* **49**, 70-83 (2010).

Acknowledgments: We thank M. Vickers for help with the X-ray diffraction measurements, J. K. Cockcroft for access to a Cryojet, Z. X. Guo for making a cryomill available, and Gabriele Sosso, Martin Fitzner, Andrew Goodwin and the late Paul F. McMillan for discussions. The authors also acknowledge the use of the UCL Kathleen High Performance Computing Facility (Kathleen@UCL) and associated support services.

Funding:

European Research Council (ERC) under the European Union's Horizon 2020 research innovation programme grant 725271 (ARF, CGS)

Austrian Science Funds (FWF) grant J4325 (AA)

Materials Chemistry Consortium grant EP/L000202 (MBD, AM)

UK Materials and Molecular Modelling Hub grants EP/P020194/1 and EP/T022213/1 (MBD, AM)

Author contributions:

Conceptualization: CGS, AS

Investigation: ARF, MBD, AA

Formal Analysis: ARF, CGS, MBD, AM

Funding acquisition: CGS, AM

Software: MBD

Visualization: ARF, CGS, MBD

Writing – original draft: CGS

Writing – review & editing: ARF, MBD, AA, AS, AM, CGS

Competing interests: Authors declare that they have no competing interests.

Data and materials availability: All data are available in the main text or the supplementary materials.

Supplementary Materials

Materials and Methods

Figs. S1 to S14